TRENDS IN SCIENCES 2026; 23(4): 11410
https://doi.org/10.48048/tis.2026.11410
RESEARCH ARTICLE

The Effect of Small Deficiency in Calcium Ion on Structural and Magnetic Properties in $La_{0.7}Ca_{0.15}\square_{0.05}Sr_{0.1}MnO_3$ with Various Synthesis Methods

Phahul Zhemas Zul Nehan[1], Marzuki Naibaho[1], Yeni Febrianti[1], Januar Widakdo[1], Maykel Manawan[2,3], Darminto Darminto[4] and Budhy Kurniawan[1,*]

[1]Study Program of Materials Science, Department of Physics, Faculty of Mathematics and Natural Science, Universitas Indonesia, Depok 16424, Indonesia
[2]Study Program of Propulsion Technology, Faculty of Defense Science and Technology, Universitas Pertahanan, Bogor 16810, Indonesia
[3]Research Center of Advanced Materials, National Research and Innovation Agency, Serpong 15314, Indonesia
[4]Department of Physics, Faculty of Science and Data Analytics, Institut Teknologi Sepuluh Nopember, Surabaya 60111, Indonesia

([*]Corresponding author's e-mail: budhy.kurniawan@sci.ui.ac.id)

Received: 28 July 2025, Revised: 18 August 2025, Accepted: 25 August 2025, Published: 20 December 2025

Abstract

We have investigated the effect of a small calcium ion deficiency and different synthesis methods on the structural and magnetic properties of the $La_{0.7}Ca_{0.15}\square_{0.05}Sr_{0.1}MnO_3$ compound. The samples were synthesized using solid-state, sol-gel, and wet-mixing methods. Structural analysis revealed that all samples exhibited a single-phase orthorhombic crystal structure with the *Pnma* space group. The lattice parameters and the MnO_6 octahedral structure changed based on the synthesis method and slight deficiency, leading to structural distortion and a mixed-valence state of Mn ions. The average crystallite sizes were 75.79, 113.98, and 107.23 nm, while the average grain sizes were 3.41, 2.06, and 1.29 μm for solid-state, sol-gel, and wet-mixing samples, respectively. FTIR confirmed the primary MnO_6 octahedral structure through Mn-O and Mn-O-Mn bonds at wavenumbers of 513 - 539 and 590 - 591 cm^{-1}. Magnetic measurements revealed the highest magnetization values of 29.50, 42.58, and 33.37 emu/g at room temperature under a 1 T magnetic field. In the meantime, the values of saturation magnetization were 37.11, 46.49, and 40.09 emu/g, as determined by the Law of Approach to Saturation method. Based on the structural and magnetic results, the sol-gel method produced the largest crystallite size and the lowest material defect level (smallest microstrain), resulting in the highest magnetization at room temperature under a 1 T magnetic field. These findings demonstrate a strong correlation between synthesis method, structural parameters, and magnetic properties.

Keywords: Magnetic materials, Perovskite manganite, Solid-state, Sol-gel, Wet-mixing

Introduction

The study of material modification has a long-standing history and continues to evolve toward developing ideal materials for specific applications. Notably, the investigation of doped perovskite manganites ($RE_{1-x}A_xMnO_3$, where RE represents rare earth elements and A denotes alkaline and alkaline earth metals) has been significantly investigated [1,2]. This interest is due to the intriguing magnetic properties of doped perovskite manganites, including colossal magnetoresistance, the magnetocaloric effect, multiferroic, magnetostriction, and microwave absorption [3,4]. The emergence of these magnetic phenomena in perovskite manganites is closely linked to the exchange interactions involving Mn ions. In the case of doped lanthanum manganite, the introduction of divalent ions such as Ca^{2+} and Sr^{2+} leads to the formation

of mixed-valence Mn ions, specifically Mn^{3+} and Mn^{4+}. The presence of Mn^{4+} facilitates double-exchange interactions in the Mn^{3+}-O^{2-}-Mn^{4+}, which partially supplants the super-exchange interactions within the Mn^{3+}-O^{2-}-Mn^{3+}. These interactions play a crucial role in altering the material's magnetic behavior from antiferromagnetic to ferromagnetic [3]. Therefore, the magnetic properties of lanthanum manganite ($LaMnO_3$) present considerable promise for diverse applications, such as magnetic refrigeration technology, sensors, spintronics, magnetic random access memory (MRAM), and cancer treatment via hyperthermia methods [3,5,6].

Magnetic properties are known to be highly sensitive to various structural parameters through material modification aimed at obtaining superior materials. The fundamental aspect of material adjustment involves heat treatment, synthesis methods, and material composition [3,7-9]. For instance, Ezaami *et al.* [10] conducted a comparison of synthesis methods between solid-state and sol-gel for $La_{0.7}Ca_{0.2}Sr_{0.1}MnO_3$ samples. They revealed that differences in synthesis methods affect structural parameters such as lattice parameters, unit cell volume, crystallite size, and grain size. The solid-state method exhibited larger grain sizes compared to the sol-gel method. In other examples, Pan *et al.* [11]; Mahjoub *et al.* [12] also compared synthesis methods between solid-state and sol-gel. They revealed that the lattice parameters and average grain size of the solid-state method were larger than sol-gel method. Additionally, several other studies comparing the effects of solid-state and sol-gel synthesis methods confirm that variations in structural parameters, primarily crystallite size, grain size, and grain distribution homogeneity, significantly contribute to the magnetic properties of the materials [13,14]. Furthermore, Munazat *et al.* [15] reported a comparison of synthesis methods for $La_{0.7}Ba_{0.1}Ca_{0.1}Sr_{0.1}MnO_3$ between sol-gel and wet-mixing methods. They noted that differences in synthesis methods influence crystallite and grain sizes, with the sol-gel samples demonstrating greater magnetization than those produced via wet-mixing, attributed to the larger grain size of the sol-gel samples. The structural parameter differences between sol-gel and wet-mixing methods arise from internal stress or defects in the structure, along with variations in mechanical and chemical treatments.

Each synthesis method has advantages and disadvantages. The solid-state method is suitable for producing ceramics with larger particle sizes, but it has weaknesses such as producing inhomogeneous particles, requiring long holding times, and high sintering temperatures for heat treatment [3,9,16]. Consequently, many researchers have alternative synthesis methods as the sol-gel method. This method can produce more uniform particle sizes. Additionally, the sol-gel method offers several advantages, including an easier production process, lower sintering temperatures, and shorter holding times than the solid-state method [10-12]. On the other hand, the wet-mixing method has not been extensively explored. However, previous studies have reported that it provides higher efficiency than the sol-gel method. This is because the wet-mixing method does not require additional precursors (such as citric acid as a metal complexing agent and ethylene glycol as a polymerization agent) and experiences less mass loss due to the absence of a combustion process [9,15,17]. Therefore, the choice of synthesis method remains a critical consideration for compound production.

The $La_{0.7}Ca_{0.2}Sr_{0.1}MnO_3$ compound has been extensively studied due to its attractive magnetic properties, such as a Curie temperature around room temperature, magnetocaloric effect, and colossal magnetoresistance phenomenon [10,18,19]. However, studies on compounds with the addition of small vacancies (□) at the A-site, specifically for the $La_{0.7}Ca_{0.2}Sr_{0.1}MnO_3$, are still limited. The presence of vacancies is expected to affect the structural and magnetic properties of the compound. For example, Chakroun *et al.* [20] reported that a small number of vacancies at the Ca^{2+} ion in $La_{0.7}Ca_{0.29}\square_{0.01}MnO_3$ affects its magnetic properties, as evidenced by a change in magnetization. These are shown by changes in magnetic properties, including magnetization value, magnetic state, and Curie temperature, which often correlate with variations in the Mn^{3+}/Mn^{4+} ion ratio. In addition, Arun *et al.* [21] also reported that adding a small number of vacancies in Sr^{2+} ions of $La_{0.67}Sr_{0.24}\square_{0.09}MnO_3$ affects structural and magnetic changes, similar to previous findings. Furthermore, this experiment serves as a continuation of the previous study conducted by Nehan *et al.* [22], which investigated the structural, magnetic, and magnetocaloric properties of $La_{0.7}Ca_{0.2-x}\square_xSr_{0.1}MnO_3$ compounds synthesized via the

solid-state method. It is believed that the change in magnetic properties is driven by structural modification due to material modification. Therefore, further investigation is needed to explore the contribution of small vacancies and variations in synthesis methods such as solid-state reaction, sol-gel, and wet-mixing to the structural and magnetic properties of $La_{0.7}Ca_{0.15}\square_{0.05}Sr_{0.1}MnO_3$ compounds.

Materials and methods

The synthesis of the compound $La_{0.7}Ca_{0.15}\square_{0.05}Sr_{0.1}MnO_3$ was conducted using several methods, including solid-state reaction, sol-gel, and wet-mixing. Details regarding the precursors used and the steps for each synthesis method are explained in the following sections. To simplify sample identification, terms such as LV-5-SSR, LV-5-SG, and LV-5-WM were adopted to represent samples produced via solid-state reaction, sol-gel, and wet-mixing methods, respectively. After dried samples were obtained from each synthesis process, they were subjected to heat treatment. The dried samples underwent calcination at 600 °C for 6 h, followed by re-grinding and pre-sintering at 900 °C for 12 h. The pre-sintered material was then re-grinded and prepared for pelletization into cylinders with a diameter of 1 cm and a thickness of 2 mm, under a pressure of 10 tons. Finally, the pelletized samples were sintered at 1,200 °C for 24 h to achieve optimal grain growth.

The process of the solid state reaction method

The precursors used to produce $La_{0.7}Ca_{0.15}\square_{0.05}Sr_{0.1}MnO_3$ are La_2O_3 (Merck), $CaCO_3$ (Merck), $SrCO_3$ (Sigma-Aldrich), and $MnCO_3$ (Sigma-Aldrich), all of high purity. The process begins with weighing all precursors according to stoichiometric calculations, followed by mixing in an agate mortar for 45 min. The well-mixed sample then proceeds to the heat treatment as outlined in the previous section.

The process of the sol-gel method

In the sol-gel method, the precursors used are La_2O_3 (Merck), $Ca(NO_3)_2{\cdot}6H_2O$ (Merck), $Sr(NO_3)_2$ (Merck), and $Mn(NO_3)_2{\cdot}4H_2O$ (Merck), all of high purity. To synthesize $La_{0.7}Ca_{0.15}\square_{0.05}Sr_{0.1}MnO_3$, each precursor is weighed according to stoichiometric calculations. The process begins with the addition of citric acid (HNO_3) to dissolve La_2O_3, while the other precursors are dissolved in distilled water. All dissolved precursors are mixed in a larger beaker. Citric acid (CA) is then added as a complexing agent, and ethylene glycol (EG) is added as a polymerization agent in a molar ratio of 1:2:4 for total metal:CA:EG, respectively. The mixture is heated to 70 - 80 °C and continuously stirred to accelerate the polyesterification reaction between CA and EG. The solution is then titrated with ammonium hydroxide until a neutral pH of 7 is achieved. The solution is kept warm until it forms a thick gel. The gel is evaporated in an oven at 190 °C overnight until a black powder is obtained. Finally, the powder is ground and prepared for the heat treatments.

The process of the wet-mixing method

In the wet-mixing method, the precursors used include La_2O_3 (Merck), $CaCO_3$ (Merck), $SrCO_3$ (Sigma-Aldrich), and $MnCO_3$ (Sigma-Aldrich), all of high purity. Each precursor is weighed according to stoichiometric calculations. The process begins with dissolving all the precursors and mixing them with a 65% nitric acid (HNO_3) solution as a solvent. The combined precursor solutions are continuously stirred while being heated to 80 °C until the solution evaporates and dries. Subsequently, the resulting powder is placed in an oven at 190 °C to ensure the removal of moisture and HNO_3. Finally, the powder is ground and prepared for the heat treatment process.

Characterizations

The characterizations of $La_{0.7}Ca_{0.15}\square_{0.05}Sr_{0.1}MnO_3$ from the 3 synthesis methods were performed to confirm their structural and magnetic properties. X-ray diffraction (XRD) patterns were obtained using Bragg-Brentano geometry on an X'pert PAN-analytical diffractometer with CuKα radiation (λ = 1.5406 Å) over a 2θ range of 10° - 90°, measured at room temperature. Morphological and elemental analyses were conducted using scanning electron microscopy-energy dispersive X-ray spectroscopy (SEM-EDS) with a Quanta 650 Thermofisher Scientific-SEM and an Xplore 15 Oxford Instruments-EDS system. The functional groups of the materials, particularly of the MnO_6 octahedral structure, were investigated using Fourier Transform Infrared Spectroscopy (FTIR) from Bruker Alpha II, covering a wavenumber range of 500 - 4,000 cm^{-1}. Magnetic

properties were studied using a Vibrating Sample Magnetometer (VSM) from the National Research and Innovation Agency of Indonesia, with measurements conducted on powder samples at room temperature and under a magnetic field of 10,000 Oe.

Results and discussion

X-ray diffraction analysis

The XRD patterns of $La_{0.7}Ca_{0.15}\square_{0.05}Sr_{0.1}MnO_3$ compounds measured at room temperature for the variations in synthesis methods: solid-state reaction, sol-gel, and wet-mixing. **Figure 1(a)** shows sharp peaks with high intensity, which are often associated with a high degree of crystallinity in the sample [22-25]. In addition, **Figure 1(b)** provides a more detailed view of the (121) crystal plane peak within the 2θ range of 32° - 33.5°, where a shift in the peak occurs at specific diffraction angles. According to Bragg's relation ($2d_{hkl}\sin\theta_{hkl} = n\lambda$), this slight peak shift indicates changes in the structural parameters of each sample [26-28]. The structural analysis of the XRD data was performed using the Rietveld refinement method with a pseudo-Voigt function in the FullProf program. All samples have a single-phase characteristic of $LaMnO_3$ phase corresponding to the orthorhombic crystal structure with the *Pnma* space group. The Rietveld analysis results are illustrated in **Figures 2(a) - 2(c)**, which compares the intensity of experimental Bragg reflection data between observed (I_{Obs}) and calculated (I_{Calc}) results, demonstrating a good fit. The XRD analysis provided several structural parameters, including phase determination, crystal structure, crystallite size, theoretical density, atomic positions, and other parameters, as summarized in **Table 1**.

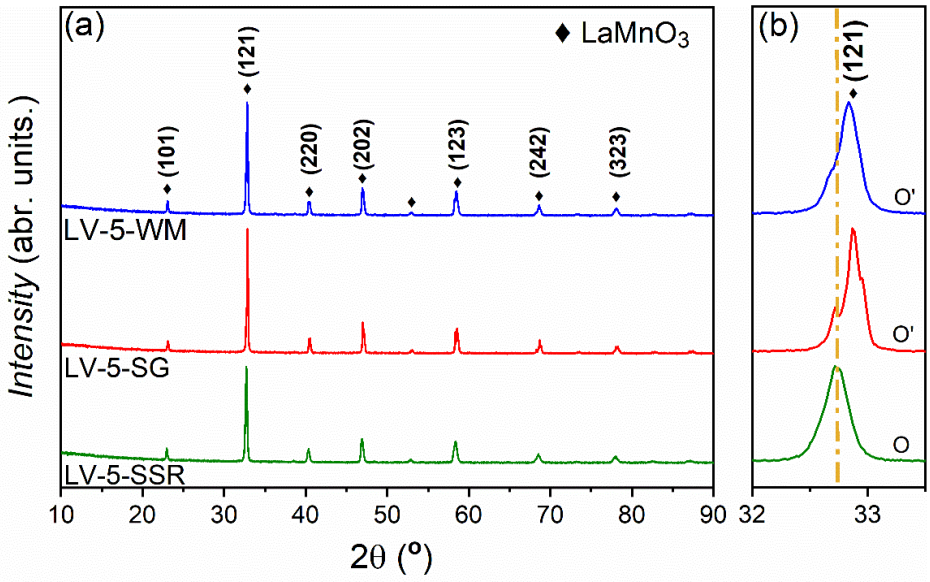

Figure 1 Powder X-ray diffraction patterns of $La_{0.7}Ca_{0.15}\square_{0.05}Sr_{0.1}MnO_3$ compounds within the 2θ range (a) 10° - 90° and (b) 32° - 33.5°.

Several prior studies have commonly employed the Goldschmidt tolerance factor (t), as expressed in Eq. (1), to estimate the crystal structure of $LaMnO_3$ phases [26,29]:

$$t = \frac{<r_A> + r_O}{\sqrt{2}(<r_B> + r_O)} \quad (1)$$

$$< r > = \Sigma x_i r_i \quad (2)$$

where $< r_A >$, $< r_B >$, and r_O represent the average ionic radii for the A, B, and oxygen sites, respectively.

All average ionic radii values were calculated using Eq. (2), utilizing the ionic radii of each ion based on the standard coordination number of nine at the A-site: La^{3+} (1.22 Å), Ca^{2+} (1.18 Å), Sr^{2+} (1.31 Å), Mn^{3+} (0.65 Å), Mn^{4+} (0.53 Å), and O^{2-} (1.38 Å) [30]. The average ionic radii calculations for all parameters are summarized in **Table 2**. Previous literature indicates that t values have several representations concerning the crystal structure of $LaMnO_3$ phases. If a value of t equal to 1 is confirmed, the crystal structure of $LaMnO_3$ is cubic. Additionally, if t falls within the range of $0.96 < t < 1$, it indicates the formation of a rhombohedral

crystal structure. Conversely, if $t < 0.96$, it represents an orthorhombic crystal structure [3,31]. The Goldschmidt tolerance factor approximations for all samples are 0.902, which is in line with the criterion of $t < 0.96$. Therefore, the results confirm that the formed crystal structure is orthorhombic, aligning with the theoretical calculations from the XRD experiments.

Table 1 Structural parameters obtained by Rietveld refinement for powder XRD patterns of $La_{0.7}Ca_{0.15}\square_{0.05}Sr_{0.1}MnO_3$ compounds with various synthesis methods.

Parameters	**LV-5-SSR**	**LV-5-SG**	**LV-5-WM**
Crystal structure	*Orthorhombic*	*Orthorhombic*	*Orthorhombic*
Space group	*Pnma*	*Pnma*	*Pnma*
$\boldsymbol{a}$ (Å)	5.4724	5.466	5.469
$\boldsymbol{b}$ (Å)	7.7406	7.724	7.731
$\boldsymbol{c}$ (Å)	5.5082	5.497	5.501
$\boldsymbol{V}$ (Å^3)	233.331	232.14	232.64
Mn_1-O_2- short (Å)	1.780	1.915	1.896
Mn_1-O_1-medium (Å)	1.952	1.931	1.933
Mn_1-O_2-long (Å)	2.104	2.044	2.046
$\mathbf{d_{<Mn-O>}}$ (Å)	1.945	1.963	1.958
Mn_1-O_1-Mn_1 (°)	164.740	178.17	178.42
Mn_1-O_2-Mn_1 (°)	176.674	156.37	159.19
< Mn-O-Mn > (°)	170.707	167.27	168.81
La/Ca/Sr (x, y, z), 4c	0.505, 0.25, 0.009	0.508, 0.25, 0.004	0.515, 0.25, 0.004
Mn (x, y, z), 4b	0, 0, 0	0, 0, 0	0, 0, 0
O_1 (x, y, z), 4c	−0.256, 0.25, −0,039	0.007, 0.25, −0.030	−0.002, 0.25, 0.004
O_2 (x, y, z), 8d	0.224, −0.005, 0.233	0.281, −0,022, 0,204	0.251, −0.044, 0.228
$< D_{W-H} >$ (nm)	75.79	113.98	107.23
$< D_{SEM} >$ (μm)	3.41	2.06	1.29
$< D_{SEM} > / < D_{W-H} >$	44.99	18.07	12.03
ε (10^{-4})	12.3	1.8	8.3
ρ_{XRD} (g/cm^3)	6.122	6.149	6.141
R_{wp} (%)	22.9	23.2	21.2
X^2 (%)	1.51	1.49	1.39

Table 2 Goldschmidt tolerance factor calculation for $La_{0.7}Ca_{0.15}\square_{0.05}Sr_{0.1}MnO_3$ compounds synthesized using solid-state reaction, sol-gel, and wet-mixing.

Parameters	**L5-SSR**	**L5-SG**	**L5-SG**
$\boldsymbol{< r_A >}$	1.2182	1.2182	1.2182
$\boldsymbol{< r_B >}$	0.6105	0.6105	0.6105
$\boldsymbol{r_O}$	1.38	1.38	1.38
$\boldsymbol{t}$	0.902	0.902	0.902

Based on **Table 1**, the lattice parameters a, b, and c show different values for each sample, while the unit cell volume tends to be constant. The LV-5-SSR sample exhibits the largest lattice parameter values, which can be attributed to the noticeable leftward shift of the main (121) peak compared to other samples. In contrast, the (121) peak of the LV-5-SG sample appears at the far right [32]. These differences in lattice parameters are clearly reflected in the peak shifts observed in the XRD patterns, as illustrated in **Figure 1(b)**. This is linked to several reasons, including (i) differences in production mechanisms, where solid-state reaction is based on dry reactions, while sol-gel and wet-mixing are based on wet reactions, and (ii) the types of precursor materials used [3,11,12]. Moreover, the dry reaction method is often associated with less uniform atomic-level homogeneity and slower atomic diffusion, which generates microstrain, as shown in **Table 1**. This, in turn, leads to higher structural defects, resulting in larger lattice parameters compared to wet-chemistry-based synthesis routes [16]. The lattice parameter values of sol-gel and wet mixing are relatively constant, which helps to understand these reasons. For instance, Ezaami et al. who investigated the effects of synthesis methods between solid-state and sol-gel for $La_{0.7}Ca_{0.2}Sr_{0.1}MnO_3$ [10], and Munazat *et al.* [15] who examined a study of synthesis comparison between sol-gel and wet-mixing for $La_{0.7}Ba_{0.1}Ca_{0.1}Sr_{0.1}MnO_3$ compounds, have also reported lattice parameter differences due to variations in the synthesis methods.

Further analysis indicates that the orthorhombic crystal structure can be categorized into 2 types based on the lattice parameters a, b, and c. If the lattice parameters satisfy the condition $\frac{b}{\sqrt{2}} > a$ and $a < c$, it indicates O-type orthorhombic distortion. Conversely, if $c > a > \frac{b}{\sqrt{2}}$, it suggests O'-type distortion [31]. The O-type distortion arises from the cooperative bending of corner-sharing octahedra, while the O'-type distortion is due to cooperative Jahn-Teller distortions associated with the rotation of MnO_6 octahedra [22,33]. The LV-5-SSR sample satisfies the criteria for exhibiting an orthorhombic O-type distortion, whereas the LV-5-SG and LV-5-WM samples exhibit an O'-type distortion. This distinction is also indicated by the (121) peak, where LV-5-SG and LV-5-WM tend to show an additional peak on the left side. In contrast, the LV-5-SSR sample, characterized by O-type distortion, displays only a single peak without any splitting. This observation is consistent with previous reports by Moreno *et al.* [18]; Sakka *et al.* [31]. **Figures 2(d) - 2(i)** display the relationship between the lattice parameters and the type of orthorhombic distortion in schematic illustrations of the crystal structure and MnO_6 octahedral structure. The presence of MnO_6 octahedral distortion indicates the characteristics of Jahn-Teller distortion in all samples [27,31]. This is strongly supported by variations in the Mn-O bond lengths, including the short Mn_1-O_2, medium Mn_1-O_1, and long Mn_1-O_2 bonds, as well as changes in the Mn_1-O_1-Mn_1 and Mn_1-O_2-Mn_1 bond angles, both of which are influenced by differences in the synthesis process [9,14,17]. The alteration of these parameters collectively indicates the presence of Jahn-Teller distortion within the complex orthorhombic crystal structure. These variations in bond lengths and angles are associated with the impact of electron transfer processes occurring within the system [15]. The crystallite size of $La_{0.7}Ca_{0.15}\square_{0.05}Sr_{0.1}MnO_3$ samples with varying synthesis methods has been estimated using peak diffraction data via the Williamson-Hall equation, as presented below [15,34]:

$$\beta\cos\theta = \frac{k\lambda}{D_{W-H}} + 4\varepsilon\sin\theta \quad (3)$$

where, D_{W-H} represents the average crystallite size calculated using the Williamson-Hall equation, k is a constant related to the sharpness factor of the crystallite (0.94), λ is the wavelength of the XRD source, β is the full width at half maximum ($FWHM$) related to the peak intensity of diffraction, θ represents the diffraction angle, and $\varepsilon = \frac{\Delta d}{d}$ is the strain coefficient [15]. This method is effectively considered as it incorporates strain broadening, reflecting the influence of synthesis processes (such as heat treatment, synthesis procedures, and milling) and defects within the crystallites (including lattice defects, doping-induced defects, and uneven atomic distribution) [34]. The value of D_{W-H} is derived from the intercept of the fitting results, while ε is obtained from the slope of the fitting. The D_{W-H} and ε values are summarized in **Table 1**. It is noteworthy

that differences in synthesis methods significantly affect crystallite size [10,16]. As reported in previous studies, the parameters D_{W-H} and ε exhibit a strong correlation [22]. A high value of ε typically indicates a significant number of defects within the material, leading to the formation of inhomogeneous crystallites and consequently resulting in a smaller D_{W-H} value. Conversely, a lower ε value suggests fewer structural defects, thereby allowing for the growth of larger crystallites and a higher D_{W-H} value [35-37]. This explanation provides a clear understanding of the observed correlation between D_{W-H} and ε in the LV-5-SSR, LV-5-SG, and LV-5-WM samples.

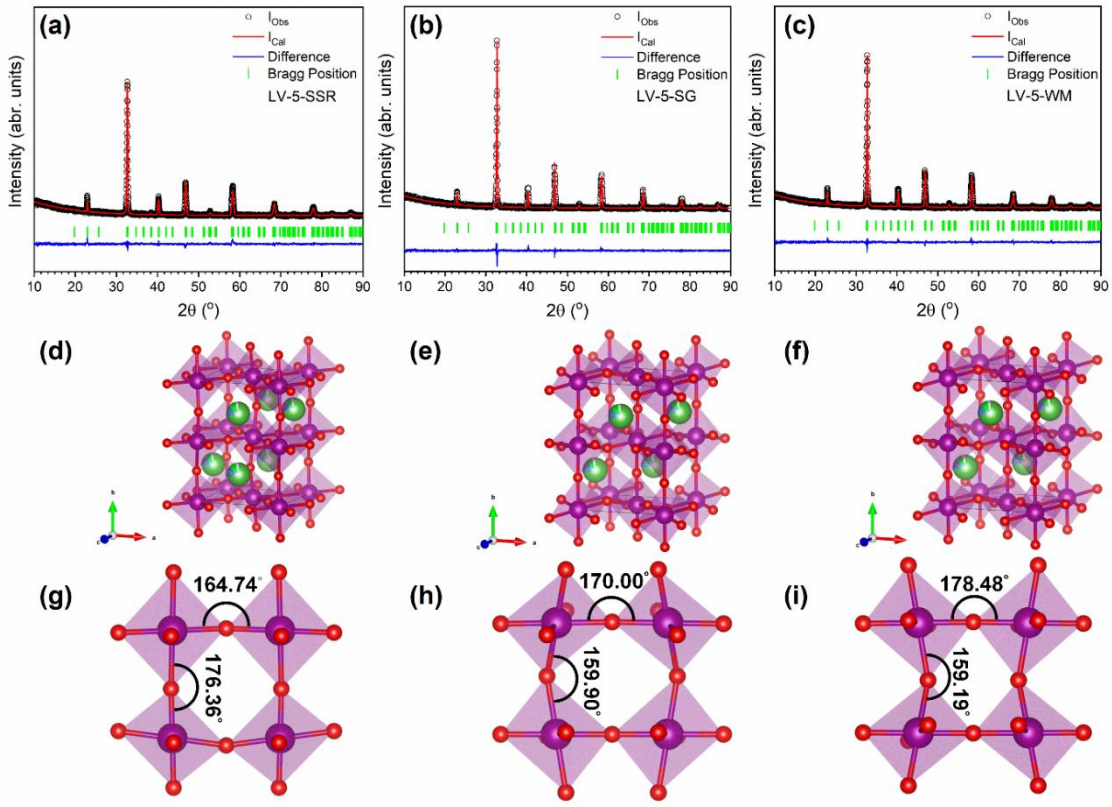

Figure 2 Rietveld refinement analysis results of XRD patterns for samples (a) LV-5-SSR, (b) LV-5-SG, (c) LV-5-WM, schematic illustration of crystal structures of (d) LV-5-SSR, (e) LV-5-SG, (f) LV-5-WM, and octahedral MnO_6 structure with Mn-O-Mn bond angles.

Furthermore, XRD data can be utilized to estimate the theoretical density using the following equation [38]:

$$\rho_{XRD} = \frac{MZ}{N_a V} \quad (4)$$

where M is the molecular mass (g/mol), Z is the number of formula units per unit cell, N_a represents Avogadro's number (6.0210×10^{23} mol^{-1}), and V is the unit cell volume obtained from XRD analysis.

The theoretical density values for each sample were 6.122, 6.149, and 6.141 g/cm^3 for LV-5-SSR, LV-5-SG, and LV-5-WM, respectively. In comparison, the parent sample $La_{0.7}Ca_{0.2}Sr_{0.1}MnO_3$ has a theoretical density of approximately 6.22 g/cm^3, while densities for samples produced via solid-state and sol-gel synthesis are around 6.20 g/cm^3 [7]. In a recent report, Nehan *et al.* [22] stated that the ρ_{XRD} value of the $La_{0.7}Ca_{0.15}\square_{0.05}Sr_{0.1}MnO_3$ compound synthesized via the solid-state reaction method was found to be 6.14 g/cm^3, indicating that the results are consistent and reproducible. Additionally, the difference in theoretical density between the parent sample and $La_{0.7}Ca_{0.15}\square_{0.05}Sr_{0.1}MnO_3$ can be understood as the introduction of vacancies at the Ca^{2+} sites reduces the overall weight of the sample while maintaining a nearly identical unit cell volume.

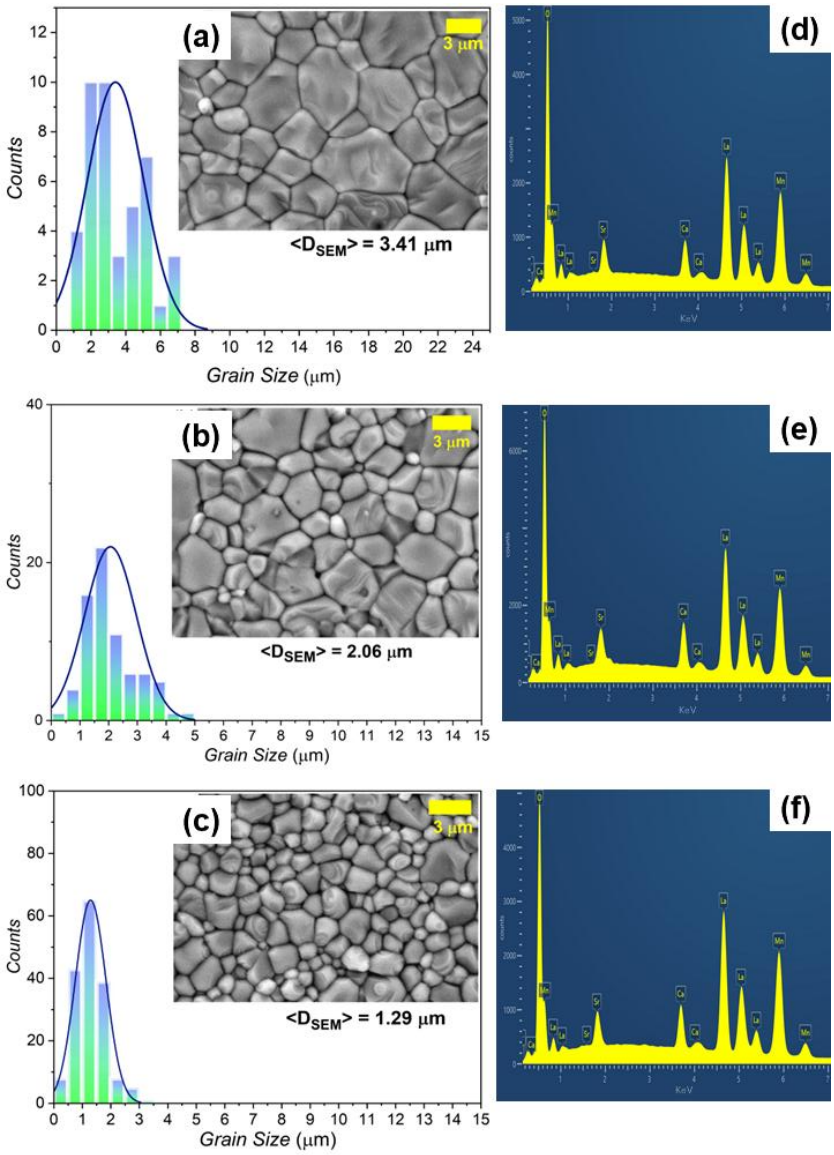

Figure 3 SEM image at 2,500× enlargement and histogram distribution of average grain size for (a) LV-5-SSR, (b) LV-5-SG, (c) LV-5-WM, and EDS spectra measurement results for (d) LV-5-SSR, (e) LV-5-SG, and (f) LV-5-WM.

Scanning electron microscope-energy dispersive X-ray spectroscopy analysis

Figure 3 presents histograms of the average grain size (D_{SEM}), and the inserted picture illustrates the surface morphology of all samples at 2,500× enlargement. Notably, the grains and grain boundaries are visible and exhibit irregular polygonal shapes with no evidence of agglomeration. This observation is consistent with previous studies on the preparation of metal oxides using solid-state reaction, sol-gel, and wet-mixing methods [10,15,39]. The D_{SEM} values for each sample were calculated using Image-J, which was used to calculate the diameter of all grains in the SEM images. The statistical analysis of the D_{SEM} is indicated by the peak of the blue distribution line.

The calculations of D_{SEM} values for LV-5-SSR, LV-5-SG, and LV-5-WM compounds are 3.41, 2.06, and 1.29 μm, respectively. These micrometer scale of D_{SEM} values are affected by the high heating factor during heat treatment (> 1,000 °C), which encourages the growth of larger grains [3,16]. The LV-5-SSR has the largest D_{SEM} with a non-homogeneous grain size distribution compared to LV-5-SG and LV-5-WM. This is related to the initial precursor being a rough powder, which allows for a slower reaction process, providing time for grain growth during heating. Prolonged

exposure to elevated temperatures leads to coarser grains due to enhanced diffusion and particle coalescence. Previous studies have reported that the absence of a melting process with chemical solutions can increase grain size [9,10]. Although both LV-5-SG and LV-5-WM were mixed with specific chemical solutions, they did not have similar D_{SEM} values owing to different chemical reactions. The differences in D_{SEM} values between LV-5-SG and LV-5-WM are often correlated to the pH conditions of the synthesis process. The sol-gel method is generally carried out under neutral conditions (pH ≈ 7), which favor more controlled hydrolysis and condensation, resulting in relatively larger particles. In contrast, the wet mixing method is performed under highly acidic conditions (pH ≈ 1), which can inhibit particle growth and promote the formation of finer grains [15,16]. Therefore, it is believed that the pH conditions and the composition of the chemical solutions play an important role in the grain size formation between LV-5-SG and LV-5-WM [15].

An important aspect to consider is the discrepancy between D_{W-H} and D_{SEM}, which is often observed in polycrystalline materials. These values may converge only when the material is synthesized at the nanoscale [35,37]. In the case of materials with micrometer-scale grain sizes, D_{W-H} and D_{SEM} typically differ, which aligns with the definition of a grain, consisting of several crystallites with similar orientations [10]. Based on this definition, the number of crystallites within a single grain can be estimated by calculating the ratio D_{SEM} and D_{W-H}, as presented in **Table 1**. This discrepancy can also be understood from the perspective of the measurement techniques employed: (i) D_{W-H} is derived from XRD data on powder samples, representing an indirect measurement based on peak broadening analysis, whereas (ii) D_{SEM} is obtained through direct observation of pelletized samples using SEM measurement, providing a visual representation of the surface morphology [25]. Therefore, these reasons explain why trends between D_{W-H} and D_{SEM} are not always in alignment [24,29

Table 3 Atomic percent of $La_{0.7}Ca_{0.15}\square_{0.05}Sr_{0.1}MnO_3$ compounds for all synthesis methods from EDS measurement results.

Elements	LV-5-SSR (at. %)	LV-5-SG (at. %)	LV-5-WM (at. %)	Stoichiometric calculation (at. %)
La	16.4	16.5	17.9	14.14
Ca	3.7	4.7	4.2	3.03
Sr	2.0	1.5	1.9	2.02
Mn	21.1	20.1	23.0	20.20
O	56.8	57.2	53.0	60.61

EDS analysis conducted on all samples revealed the presence of La, Ca, Sr, Mn, and O, confirming the consistency of these elements with the employed chemical formula. The spectra of La, Ca, Sr, Mn, and O elements are illustrated in **Figures 3(d)** - **3(e)**. Additionally, semi-quantitative calculations of each element measured on the sample surfaces are summarized in **Table 3**, which compares these results with stoichiometric calculations. These discrepancies of data demonstrate the alignment between the expected and measured compositions, affirming the success of the applied synthesis methods. On the other hand, the La and Ca exhibit higher at % experimental content than stoichiometric. It can be caused by this surface-sensitive technique that can be influenced by local inhomogeneity, surface segregation, and instrumental error. Moreover, the EDS technique is performed for scanning only on the surface area of samples, which does not directly represent bulk site occupancy. The evidence for Ca-site vacancies is derived from bulk-sensitive Rietveld refinement of XRD patterns using the atom formation of $La_{0.7}Ca_{0.15}\square_{0.05}Sr_{0.1}MnO_3$. It is supported by the presence of the MnO_6 octahedral structure distortion in the systems. Furthermore, the detailed element distributions of compounds are captured in the mapping SEM images, as shown in **Figure 4**.

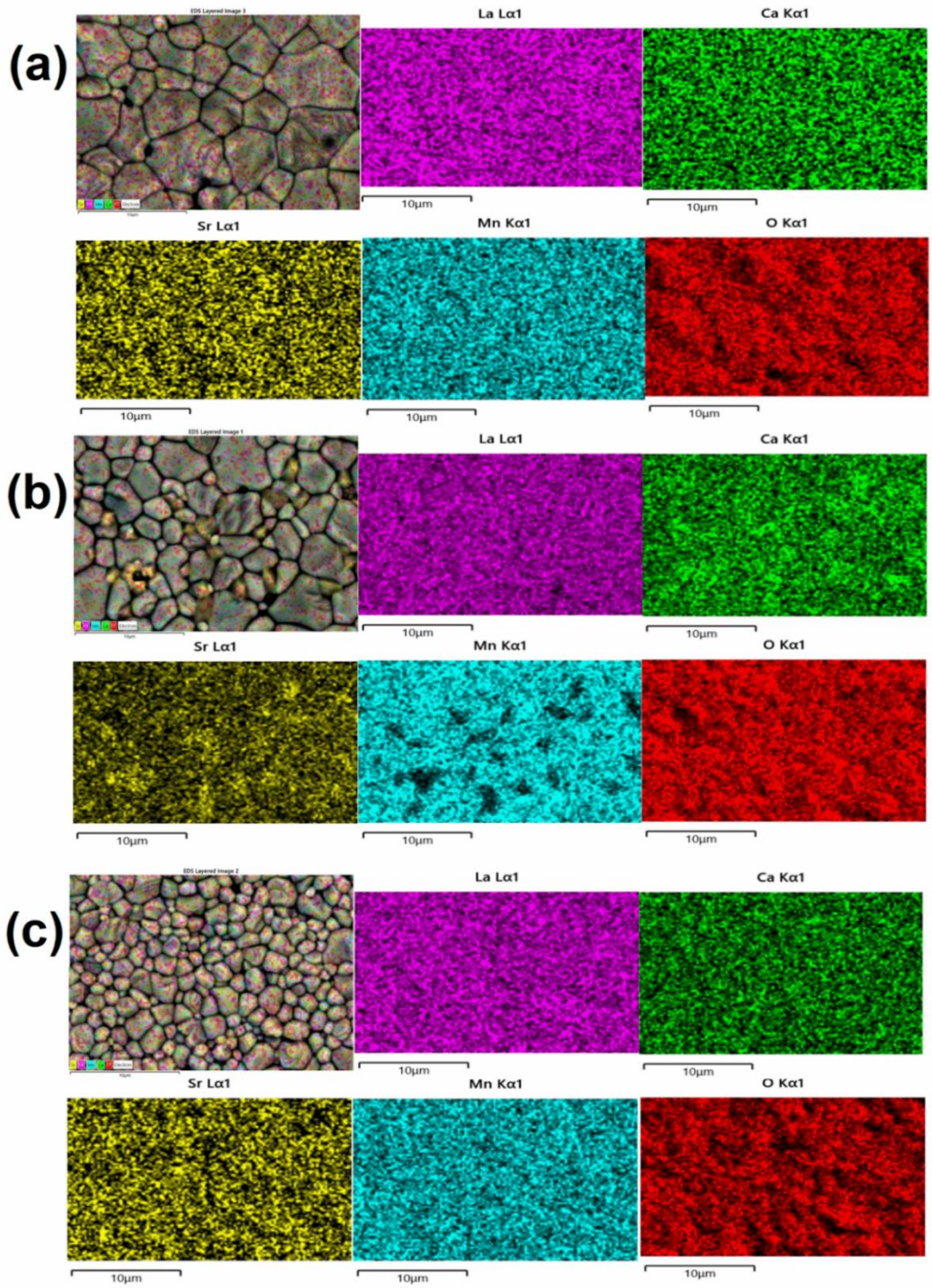

Figure 4 Elemental distribution maps, obtained through EDS measurement, for compounds (a) LV-5-SSR, (b) LV-5-SG, and (c) LV-5-WM. These maps illustrate the elemental distribution of Lanthanum (purple), Calcium (green), Strontium (yellow), Manganese (cyan), and Oxygen (red). Such analysis provides valuable insights into the composition and homogeneity of the samples.

Fourier transform infrared spectroscopy analysis

Figure 5 presents the FTIR spectra of the compounds LV-5-SSR, LV-5-SG, and LV-5-WM, measured in the wavenumber range of 500 - 4,000 cm^{-1} at room temperature. Previous studies have often associated the presence of the MnO_6 octahedral structure in $LaMnO_3$ with octahedral symmetry, characterized by 2 infrared bands at 400 and 600 cm^{-1} [10,40,41]. The absorption dips in the band between 513 and 534 cm^{-1}

are linked to the internal bending mode, resulting from changes in the Mn-O-Mn bond angles [41]. Second absorption dips in the wavenumber range of 590 - 591 cm^{-1} are associated with the asymmetric stretching mode of the Mn-O-Mn and Mn-O bonds, which is characteristic of the MnO_6 octahedron formation in all samples [10,22,40]. The spectra indicate a reduction in peak intensity at different wavenumbers, correlating with variations in Mn-O bond lengths, Mn-O-Mn bond angles, and unit cell volumes derived from XRD analysis [40,41]. Additionally, the FTIR spectra display stretching vibrations of C=O and C-O in the wavenumber range of 990 - 1,132 cm^{-1}, attributed to carbon residues remaining from the combustion during the heating treatment and FTIR preparation for all samples [40,42]. Notably, the LV-5-SG sample exhibits lower peak intensity in the range of 990 - 1,132 cm^{-1} compared to the other 2 samples, indicating a reduced carbon residue in this sample. Furthermore, the presence of peaks in the range of 2,000.00 - 2,400.00 cm^{-1} suggests the presence of CO_2, likely due to the natural porosity of the samples [43,44]. The summary of FTIR information is tabulated in **Table 4**.

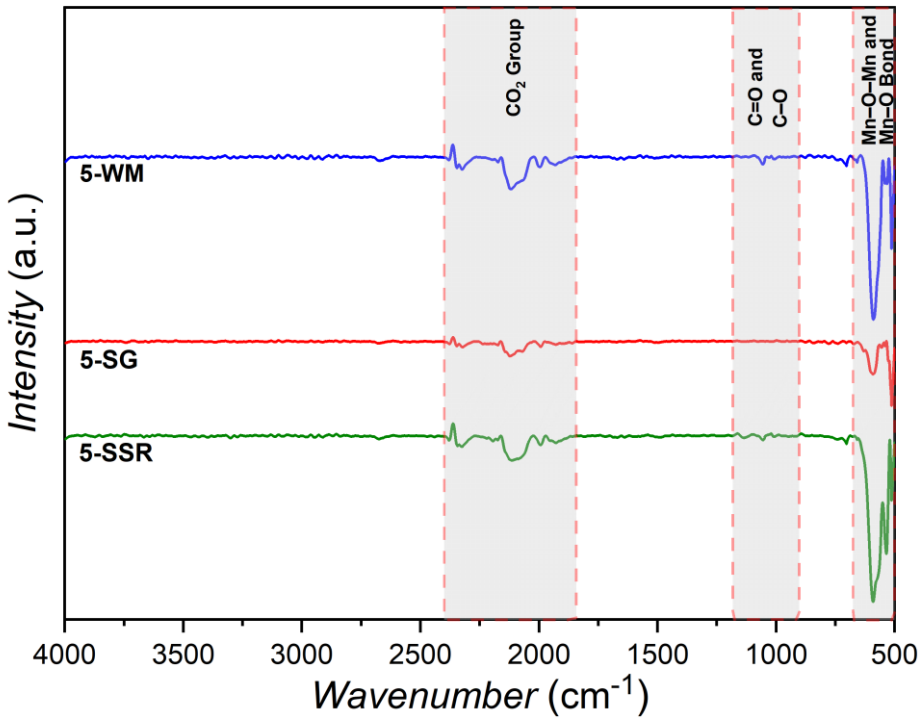

Figure 5 FTIR spectra from $La_{0.7}Ca_{0.15}\square_{0.05}Sr_{0.1}MnO_3$ compounds for all synthesis methods with wavenumber range of 500 - 4,000 cm^{-1}.

Table 4 Peak positions of absorption bands from FTIR measurements of $La_{0.7}Ca_{0.15}\square_{0.05}Sr_{0.1}MnO_3$ compounds in the wavenumber range 4,000 - 500 cm^{-1}.

Wavenumber rang (cm^{-1})	Attributed to
513 - 534	Bending mode vibration of Mn-O-Mn bond angle [10,40,41]
590 - 591	Stretching mode vibrations of Mn-O and Mn-O-Mn bonds [10,40]
990 - 1,132	Stretching mode vibrations of C=O and C-O bonds, indicating the presence of carbon [40,42]
2,000 - 2,400	Presence of CO_2 functional group [43,44]

Magnetic properties of $La_{0.7}Ca_{0.15}\square_{0.05}Sr_{0.1}MnO_3$ compounds

Magnetic properties were investigated by measuring the magnetization of the $La_{0.7}Ca_{0.15}\square_{0.05}Sr_{0.1}MnO_3$ compound under an applied magnetic field of 10,000 Oe at room temperature. **Figure 6** presents the magnetization versus magnetic field ($M(\mu_0 H)$) curves obtained from VSM

measurements. The maximum magnetization values (M_{max}) at a magnetic field of 1 T for samples LV-5-SSR, LV-5-SG, and LV-5-WM were found to be 29.50, 42.58, and 33.37 emu/g, respectively. The magnetization behavior of $La_{0.7}Ca_{0.15}\square_{0.05}Sr_{0.1}MnO_3$ correlates with the aligned magnetic field, affecting an increase in magnetization values [45]. All samples exhibited ferromagnetic behavior with soft-magnetic characteristics, as the magnetic properties of $LaMnO_3$ [15,46]. This is indicated by the coercivity (H_C) and remanence (M_r) values summarized in **Table 5**. Notably, the magnetization of sample LV-5-SG was higher than that of LV-5-SSR and LV-5-WM. Previous studies have reported several critical parameters influencing the reduction in magnetization, including (i) grain size, (ii) crystallite size, (iii) structural defects, (iv) weakening of ferromagnetic states (due to the Mn^{3+}-O^{2-}-Mn^{4+}, double-exchange interaction), and the presence of antiferromagnetic states (from the Mn^{3+}-O^{2-}-Mn^{3+}, super-exchange interaction) resulting from the Mn^{3+}/Mn^{4+} ratio influenced by the synthesis process, and (v) inhomogeneity in grain and crystallite size distribution [3,13,47]. Yadav *et al.* [47] noted that an increase in grain size in samples can reduce the non-magnetic layers, contributing to an increase in magnetization, and *vice versa*. However, structural defects and inhomogeneity in grain size distribution are characteristic of the solid-state reaction method, where the slow grain growth process leads to inhomogeneity and structural defects, thereby reducing magnetization [10,16]. Additionally, this argument is supported by the highest ε values for LV-5-SSR, which may indicate massive defects in the compounds. In contrast, the LV-5-SG and LV-5-WM samples exhibited a more homogeneous grain size distribution and relatively low ε values, reducing defects due to the use of acid-based chemical solutions [35,37]. The homogeneity of grain size distribution for each sample is illustrated in the SEM images shown in **Figures 3(a) - 3(c)**. It is important to note that differences in synthesis methods can contribute to changes in magnetic properties associated with variations in structural parameters.

As shown in **Figure 6**, all samples measured under a magnetic field of 10,000 Oe do not exhibit saturation magnetization. Several studies reported that the saturation magnetization will be captured in a very high magnetic field [45,48]. Although saturation magnetization values are not known from the experimental data, we can gain detailed information about the magnetic properties (including saturation magnetization (M_S), effective magnetocrystalline anisotropy constant (K_{eff}), and anisotropy field (H_a)) utilizing the Law of Approach to Saturation (LAS) method. The equation of LAS method can be written as follows [49,50]:

$$M = M_S\left(1 - \frac{A}{\mu_0 H} - \frac{B}{\mu_0 H^2}\right) + \chi\mu_0 H \quad (5)$$

$$B = \frac{4K_{eff}^2}{15M_S^2} \quad (6)$$

$$H_a = \frac{2K_{eff}}{M_s} \quad (7)$$

In this context, A is a constant reflecting inhomogeneity parameter, B corresponds to the anisotropy factor, $\mu_0 H$ is the applied magnetic field, and χ represents the magnetic susceptibility. Furthermore, $\frac{A}{H}$ determines the inhomogeneity of materials, $\frac{B}{H^2}$ refers to against the magneto-crystalline anisotropy, and $\chi\mu_0 H$ is known as a paramagnetism-like term [51]. It is generally accepted that the $\chi\mu_0 H$ term becomes relevant only under high-temperature conditions and vanishes in high-field conditions [50,52]. Consequently, for measurements conducted at room temperature, this term can be omitted due to its minimal contribution. Thus, in these calculations, consider not using $\chi\mu_0 H$ parameter.

Figure 7 exhibits the fitting results of the $M(\mu_0 H)$ curves based on the LAS method within the magnetic field range of 4,000 - 1,0000 Oe for all compounds. The calculated values of K_{eff} and H_a show different values, indicating that the synthesis method strongly influences the magnetic properties of the compounds. It is observed that the trend of all parameters obtained from the LAS fitting is consistent with the experimental magnetic properties. This is in agreement with the reported research by Jithin *et al.* [53] on $La_{1-x}Ca_xMnO_3$ compounds, where a higher K_{eff} typically results in a reduced calculated saturation magnetization M_S. The variation in K_{eff} among samples is primarily attributed to differences in structural parameters. In this context, grain size and crystallite size play a critical role in

determining the magnitude of K_{eff}. As grain and crystallite sizes decrease, accompanied by an increase in material defects, the surface-to-volume ratio becomes larger, enhancing the contribution of surface anisotropy. This anisotropy arises due to atoms at the surface experiencing a different bonding environment compared to those within the bulk. Consequently, smaller grains and crystallites with high defect concentrations tend to exhibit higher K_{eff} values. In contrast, larger particles are more influenced by the intrinsic properties of the material and its crystal structure [54]. A similar trend is observed for the H_a parameter, as it is directly correlated with K_{eff}. A comprehensive summary of the magnetic parameters obtained from the LAS method is provided in **Table 5**.

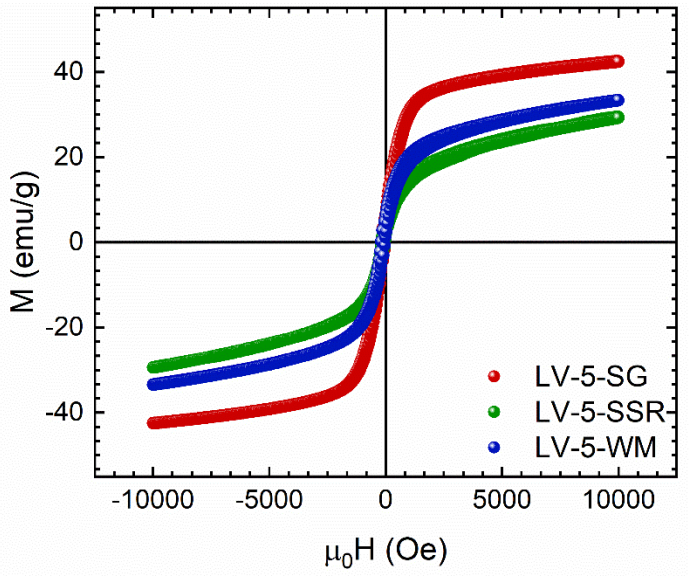

Figure 6 Magnetization versus magnetic field curves via VSM measurements of $La_{0.7}Ca_{0.15}\square_{0.05}Sr_{0.1}MnO_3$ compounds for all synthesis method variations.

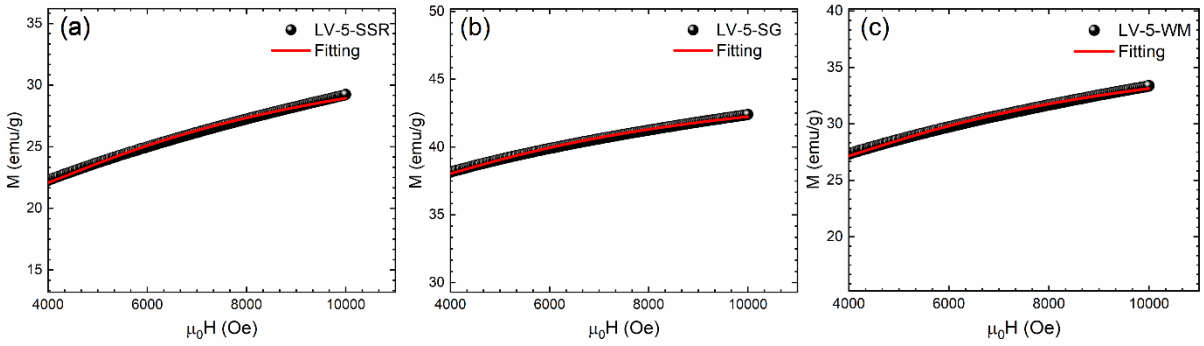

Figure 7 Magnetization versus magnetic field curves of samples (a) LV-5-SSR, (b) LV-5-SG, and (c) LV-5-WM with the magnetic field range of 400 - 10,000 Oe, fitted using the Law of Approach to Saturation method.

Table 4 Magnetic parameters of the $La_{0.7}Ca_{0.15}\square_{0.05}Sr0._1MnO_3$ compounds compared with previous reports.

Sample	Synthesis Method *	$\mu_0 H$ (T)	M_{max} (emu/g)	M_r (emu/g)	H_C (Oe)	Reference
$La_{0.7}Ca_{0.15}\square_{0.05}Sr_{0.1}MnO_3$	SSR	1	29.50	4.81	0.018	This Work
$La_{0.7}Ca_{0.15}\square_{0.05}Sr_{0.1}MnO_3$	SG	1	42.58	6.54	0.019	This Work

Sample	Synthesis Method *	$\mu_0 H$ (T)	M_{max} (emu/g)	M_r (emu/g)	H_C (Oe)	Reference
$La_{0.7}Ca_{0.15}\square_{0.05}Sr_{0.1}MnO_3$	WM	1	33.37	5.53	0.019	This Work
$La_{0.7}Ca_{0.3}MnO_3$	HEBM	2	~10	-	-	[18]
$La_{0.7}Ca_{0.25}Sr_{0.05}MnO_3$	HEBM	2	~18	-	-	[18]
$La_{0.7}Ca_{0.2}Sr_{0.1}MnO_3$	HEBM	2	~40	-	-	[18]
$La_{0.7}Ca_{0.15}Sr_{0.15}MnO_3$	HEBM	2	~57	-	-	[18]
$La_{0.7}Ca_{0.1}Sr_{0.2}MnO_3$	HEBM	2	~65	-	-	[18]
$La_{0.67}Sr_{0.33}MnO_3$	SSR	0.9	~67.5	-	-	[21]
$La_{0.67}Sr_{0.24}\square_{0.09}MnO_3$	SSR	0.9	~66	-	-	[21]
$La_{0.67}Sr_{0.15}\square_{0.18}MnO_3$	SSR	0.9	~56	-	-	[48]
$La_{0.67}Sr_{0.06}\square_{0.27}MnO_3$	SSR	0.9	~41	-	-	[48]
$La_{0.7}Ca_{0.24}Sr_{0.06}MnO_3$	SG	0.7	~60	-	-	[55]
$La_{0.7}Ca_{0.205}Sr_{0.095}MnO_3$	SG	0.7	~66	~2.5	~31	[55]
$La_{0.7}Ca_{0.25}Sr_{0.05}MnO_3$	SG	~0.25	~5	-	-	[56]
$La_{0.7}Ca_{0.2}Sr_{0.1}MnO_3$	SG	~0.25	~54	9.9	16.5	[56]
$La_{0.7}Ca_{0.1}Sr_{0.2}MnO_3$	SG	~0.25	~61	17.5	30.9	[56]
$La_{0.7}Sr_{0.3}MnO_3$	SG	~0.25	~66	19.9	36.7	[56]

(*) Note: SSR = solid-state reaction, SG = sol-gel, HEBM = high energy ball milling.

Therefore, it can be understood that differences in processing, particularly the synthesis method, have a significant impact on both the structural parameters and the magnetic properties of the compounds. Additionally, the introduction of a slight calcium deficiency in $La_{0.7}Ca_{0.15}\square_{0.05}Sr_{0.1}MnO_3$ compounds offers a new perspective on compound formation, which is predicted to enhance the magnetic properties, consistent with several previous reports [20,22,57]. It is expected that the findings of this study can serve as a valuable reference and a potential candidate for the future development of magnetic-based applications, such as active magnetic refrigeration, magnetic sensors, MRAM, and related technologies [3].

Table 5 Magnetic parameters of the $La_{0.7}Ca_{0.15}\square_{0.05}Sr0_{.1}MnO_3$ compounds approached by the LAS method.

Sample	M_S (emu/g)	M_r/M_S	$K_{eff}\times10^3$ (erg/cm^3)	$H_a\times10^4$ (Oe)	B×10^2 (Oe)
LV-5-SSR	37.11	0.154	1.77	7.64	3.89
LV-5-SG	46.49	0.163	0.92	4.96	1.64
LV-5-WM	40.09	0.165	1.34	6.68	2.98

Conclusions

In this summary, $La_{0.7}Ca_{0.15}\square_{0.05}Sr_{0.1}MnO_3$ compounds were successfully synthesized via solid-state reaction, sol-gel, and wet-mixing methods. All samples have a single-phase orthorhombic crystal structure with *Pnma* space group. The XRD patterns exhibited sharp peaks with high intensity, indicating good crystallinity. The average crystallite sizes of the samples were 75.79, 113.98, and 107.23 nm, while the average grain sizes were 3.41, 2.06, and 1.29 μm for LV-5-SSR, LV-5-SG, and LV-5-WM, respectively. The difference between these crystallite and grain sizes is connected to the diverse observations, in which crystallite size is calculated using indirect XRD

measurement, and grain size is calculated using direct SEM measurement. The Mn-O stretching and Mn-O-Mn bending vibrations, confirmed by FTIR peaks at 513 - 534 and 590 - 591 cm^{-1}, verified the preservation of the MnO_6 octahedral structure in the samples. The investigation of magnetic properties revealed ferromagnetic behavior with soft magnetic type (low coercivity), characterized by high magnetization values of 29.50, 42.58, and 33.37 emu/g for LV-5-SSR, LV-5-SG, and LV-5-WM, respectively. The calculation of saturation magnetization approximately uses LAS methods with the values of 37.11, 46.49, and 40.09 emu/g for LV-5-SSR, LV-5-SG, and LV-5-WM, respectively. LV-5-SG revealed the highest maximum magnetization at room temperature under a 1 T magnetic field. These magnetic properties correlated with large crystallite size, low defect, and the possible Jahn-Teller distortion via the MnO_6 octahedral structure. The observed relationship between synthesis routes and slight calcium ion deficiency-dependent structural parameters (lattice parameters, crystallite size, Mn-O length, and Mn-O-Mn angle bond characteristics) and magnetic properties underscores the strong double exchange-interaction in this system for producing ferromagnetic behavior. These results demonstrate that both synthesis method and Ca ion deficiency can be used as effective tools to tailor structural and magnetic behavior in perovskite manganites. Therefore, this study offers a new perspective on the impact of synthesis methods and calcium ion deficiency in perovskite manganite materials for future applications such as magnetic refrigeration, MRAM, and spintronics.

Acknowledgements

The authors gratefully acknowledged the PMDSU Scholarship for Phahul Zhemas Zul Nehan, and this study was supported by the Faculty of Mathematics and Natural Sciences, Universitas Indonesia, under research grant Hibah Publikasi Pascasarjana FMIPA UI 2024 with contract number PKS-045/UN2.F3.D/PPM.00.02/2024.

Declaration of Generative AI in Scientific Writing

During the preparation of this manuscript paper, the author used Grammarly to improve the manuscript's readability and language. After using this tool, the author reviewed and edited all content as needed and took full responsibility for the content of the publication.

CRediT Author Statement

Phahul Zhemas Zul Nehan: Conceptualization; Writing - original draft; Writing - review & editing; Investigation; Formal analysis; Software and Visualization. **Marzuki Naibaho:** Resources and Investigation. **Yeni Febrianti:** Investigation. **Januar Widakdo:** Writing - review & editing; Validation and Data Curation. **Maykel Manawan:** Supervision; Software; Validation and Writing - Review & Editing. **Darminto Darminto:** Writing - Reviewing and Editing; Supervision and Validation. **Budhy Kurniawan:** Methodology; Validation; Writing - Review & Editing; Supervision; Project administration and Funding acquisition.

References

[1] AD Souza, S Rayaprol, A Sagdeo, AK Sinha and M Daivajna. Magnetic phase transformation in $La_{0.7-x}Bi_xSr_{0.3}MnO_3$ ($0.25 \leq x \leq 0.40$). *Journal of Magnetism and Magnetic Materials* 2020; **511**, 166966.

[2] M Wali, A Hajji, R Dhahri, E Dhahri and F Sahnoune. Enhancement of the magnetocaloric effect by deficit in A site at room temperature and correlation with transport properties. *Solid State Communications* 2024; **391**, 115630.

[3] PZZ Nehan, O Vitayaya, DR Munazat, MTE Manawan, D Darminto and B Kurniawan. The magnetocaloric effect properties for potential applications of magnetic refrigerator technology: A review. *Physical Chemistry Chemical Physics* 2024; **26(20)**, 14476-14504.

[4] H Gu, X Zhang, H Wei, Y Huang, S Wei and Z Guo. An overview of the magnetoresistance phenomenon in molecular systems. *Chemical Society Reviews* 2013; **42(13)**, 5907-5943.

[5] O Vitayaya, PZZ Nehan, DR Munazat, MTE Manawan and B Kurniawan. Magnetoresistance (MR) properties of magnetic materials. *RSC Advances* 2024; **14(26)**, 18617-18645.

[6] A Kitanovski. Energy applications of magnetocaloric materials. *Advanced Energy Materials* 2020; **10(10)**, 1903741.

[7] A Ezaami, E Sellami-Jmal, I Chaaba, W Cheikhrouhou-Koubaa, A Cheikhrouhou and EK Hlil. Effect of elaborating method on magnetocaloric properties of $La_{0.7}Ca_{0.2}Ba_{0.1}MnO_3$ manganite. *Journal of Alloys and Compounds* 2016; **685**, 710-719.

[8] S Hcini, N Kouki, A Omri, A Dhahri and ML Bouazizi. Effect of sintering temperature on structural, magnetic, magnetocaloric and critical behaviors of Ni-Cd-Zn ferrites prepared using sol-gel method. *Journal of Magnetism and Magnetic Materials* 2018; **464**, 91-102.

[9] PZZ Nehan, O Vitayaya, DR Munazat, M Naibaho, M Manawan, D Darminto and B Kurniawan. A comparison study on structural properties in $La_{0.7}Ca_{0.2}Sr_{0.1}MnO_3$ compound synthesized by solid-state, sol-gel, and wet-mixing methods. *Materials Science Forum* 2025; **1152**, 45-54.

[10] A Ezaami, NO Nasser, W Cheikhrouhou-Koubaa, M Koubaa, A Cheikhrouhou and EK Hlil. Physical properties of $La_{0.7}Ca_{0.2}Sr_{0.1}MnO_3$ manganite: A comparison between sol-gel and solid state process. *Journal of Materials Science: Materials in Electronics* 2017; **28(4)**, 3648-3658.

[11] S Mahjoub, M Baazaoui, EK Hlil and M Oumezzine. Effect of synthesis techniques on structural, magnetocaloric and critical behavior of $Pr_{0.6}Ca_{0.1}Sr_{0.3}Mn_{0.975}Fe_{0.025}O_3$ manganites. *Ceramics International* 2015; **41(9)**, 12407-12416.

[12] KY Pan, SA Halim, KP Lim, W Daud, SK Chen and M Navasery. Microstructure, electrical and magnetic properties of polycrystalline $La_{0.85}K_{0.15}MnO_3$ manganites prepared by different synthesis routes. *Journal of Materials Science: Materials in Electronics* 2013; **24(6)**, 1869-1874.

[13] P Suresh and S Srinath. Effect of synthesis route on the multiferroic properties of $BiFeO_3$: A comparative study between solid state and sol-gel methods. *Journal of Alloys and Compounds* 2015; **649**, 843-850.

[14] MMB Rejeb, Y Regaieg, A Marzouki-Ajmi, W Cheikhrouhou-Koubaa, S Ammar-Merah, A Cheikhrouhou and T Mhiri. A comparative study of $La_{0.65}Ca_{0.2}(Na_{0.5}K_{0.5})_{0.15}MnO_3$ compound synthesized by solid-state and sol-gel process. *Journal of Alloys and Compounds* 2017; **695**, 2597-2604.

[15] DR Munazat, B Kurniawan, DS Razaq, K Watanabe and H Tanaka. Crossover critical behavior and magnetic entropy change of $La_{0.7}Ba_{0.1}Ca_{0.1}Sr_{0.1}MnO_3$: A comparison between wet-mixing and sol-gel synthesis methods. *Physica B: Condensed Matter* 2020; **592**, 412227.

[16] VE Salazar-Muñoz, AL Guerrero and SA Palomares-Sánchez. Review of magnetocaloric properties in lanthanum manganites. *Journal of Magnetism and Magnetic Materials* 2022; **562**, 169787.

[17] O Vitayaya, B Kurniawan, PZZ Nehan, DR Munazat, T Sudiro, A Imaduddin, H Nugraha, SD Yudanto and MTE Manawan. Enhanced magnetoresistance properties of K-site deficient $La_{0.85}K_{0.1}\square_{0.05}MnO_3$ manganites synthesized via sol-gel, wet-mixing, and solid-state reaction methods. *RSC Advances* 2024; **14(52)**, 38615-38633.

[18] CA Taboada-Moreno, F Sánchez-De Jesús, F Pedro-García, CA Cortés-Escobedo, JA Betancourt-Cantera, M Ramírez-Cardona and AM Bolarín-Miró. Large magnetocaloric effect near to room temperature in Sr doped $La_{0.7}Ca_{0.3}MnO_3$. *Journal of Magnetism and Magnetic Materials* 2020; **496**, 165887.

[19] T Sun, S Zhao, F Ji and X Liu. Enhanced room-temperature MR and TCR in polycrystalline $La_{0.67}(Ca_{0.33-x}Sr_x)MnO_3$ ceramics by oxygen assisted sintering. *Ceramics International* 2018; **44(2)**, 2400-2406.

[20] J Makni-Chakroun, W Cheikhrouhou-Koubaa, M Koubaa and A Cheikhrouhou. Impact of a small amount of vacancy in both lanthanum and calcium on the physical properties of nanocrystalline $La_{0.7}Ca_{0.3}MnO_3$ manganite. *Journal of Alloys and Compounds* 2015; **650**, 421-429.

[21] B Arun, VR Akshay and M Vasundhara. Observation of enhanced magnetocaloric properties with A-site deficiency in $La_{0.67}Sr_{0.33}MnO_3$ manganite. *Dalton Transactions* 2018; **43**, 15512-15522.

[22] PZZ Nehan, B Kurniawan, DR Munazat, O Vitayaya, M Naibaho, T Sudiro, MTE Manawan, D Darminto and H Nojiri. Calcium ion deficiency and its influence on structure, critical behavior, magnetic and magnetocaloric effect properties in $La_{0.7}Ca_{0.2-x}\square_xSr_{0.1}MnO_3$ (x = 0.00, 0.05, and 0.10) manganites. *Journal of Alloys and Compounds* 2025; **1020**, 179467.

[23] X Lu, W Chen, S Tang, J Xu, Y Zeng, X Wang, X Peng, J Li and B Hong. Tuning the microstructure and magnetocaloric properties of Na^+-substituted $La_{0.67}Ca_{0.33-x}Na_xMnO_3$ porous nanospheres. *Journal of Alloys and Compounds* 2024; **976**, 173016.

[24] K Laajimi, M Khlifi, EK Hlil, K Taibi, MH Gazzah and J Dhahri. Room temperature magnetocaloric effect and critical behavior in $La_{0.67}Ca_{0.23}Sr_{0.1}Mn_{0.98}Ni_{0.02}O_3$ oxide. *Journal of Materials Science: Materials in Electronics* 2019; **30(13)**, 11868-11877.

[25] MZ Kurt, S Kılıç Çetin, A Kandemir, G Akça, F Karadağ and A Ekicibil. Enhancement of magnetocaloric effect by partial substitution of Bi in $La_{0.60}Dy_{0.10}Sr_{0.30}Mn_{(1-x)}Bi_xO_3$ manganites (x = 0, 0.01, 0.03, and 0.10). *Journal of Materials Science: Materials in Electronics* 2024; **35(8)**, 565.

[26] DR Munazat, B Kurniawan, N Kurita, X Wang, M Manawan, T Sudiro and H Nojiri. Investigation of A-site cation disorder on structure, magnetic properties, and magnetic entropy change of trisubstituted divalent ion in $La_{0.7}(Ba,Ca,Sr)_{0.3}MnO_3$ manganite. *Physical Chemistry Chemical Physics* 2024; **26(14)**, 111-114.

[27] M Debnath, E Bose, D Biswas and S Pal. Effects on magnetocaloric and magnetoresistive properties due to nonmagnetic Zn^{2+} substitution at Mn-site in charge-ordered $Pr_{0.5}Ca_{0.5}MnO_3$ manganite. *Journal of Alloys and Compounds* 2024; **1004**, 175704.

[28] R Kumar and M Kar. Correlation between lattice strain and magnetic behavior in non-magnetic Ca substituted nano-crystalline cobalt ferrite. *Ceramics International* 2016; **42(6)**, 6640-6647.

[29] G Singh, A Gaur, P Bisht and RN Mahato. Effect of bismuth doping on structural, morphological, Griffiths-like phase, and magnetocaloric properties in $La_{0.9-x}Bi_xBa_{0.1}MnO_3$ (x = 0, 0.05, and 0.1). *Journal of Magnetism and Magnetic Materials* 2024; **591**, 171731.

[30] RD Shannon and CT Prewitt. Revised values of effective ionic radii. *Structural Science* 1970; **26(7)**, 1046-1048.

[31] A Sakka, R M'nassri, MM Nofal, S Mahjoub, W Cheikhrouhou-Koubaa, N Chniba-Boudjada, M Oumezzine and A Cheikhrouhou. Structure, magnetic and field dependence of magnetocaloric properties of $Pr_{0.5}RE_{0.1}Sr_{0.4}MnO_3$ (RE = Eu and Er). *Journal of Magnetism and Magnetic Materials* 2020; **514**, 167158.

[32] AM Zhang, WC Zhang, XS Wu and JG Lin. Abnormal enhancement of ferromagnetism for $LaMnO_{3+\delta}$ thin films with decreasing oxygen pressure. *AIP Advances* 2017; **7(5)**, 055837.

[33] B Sudakshina, KD Chandrasekhar, HD Yang and M Vasundhara. Observation of complex magnetic behaviour in calcium doped neodymium manganites. *Journal of Physics D: Applied Physics* 2017; **50(6)**, 065004.

[34] MS Hossain and S Ahmed. Easy and green synthesis of TiO_2 (Anatase and Rutile): Estimation of crystallite size using Scherrer equation, Williamson-Hall plot, Monshi-Scherrer Model, size-strain plot, Halder- Wagner Model. *Results in Materials* 2023; **20**, 100492.

[35] D Nath, F Singh and R Das. X-ray diffraction analysis by Williamson-Hall, Halder-Wagner and size-strain plot methods of CdSe nanoparticles - a comparative study. *Materials Chemistry and Physics* 2020; **239**, 122021.

[36] T Ungár. Microstructural parameters from X-ray diffraction peak broadening. *Scripta Materialia* 2004; **51(8)**, 777-781.

[37] AK Zak, WHA Majid, ME Abrishami and R Yousefi. X-ray analysis of ZnO nanoparticles by Williamson-Hall and size-strain plot methods. *Solid State Sciences* 2011; **13(1)**, 251-256.

[38] C Henchiri, R Hamdi, T Mnasri, MA Valente, PR Prezas and E Dhahri. Structural and magnetic properties of $La_{1-x}\square_xMnO_3$ (x = 0.1; 0.2 and 0.3) manganites. *Applied Physics A* 2019; **125(10)**, 725.

[39] B He, Z Zou, W Zhang, X Jiang and Z Mao. Physical explanation of magnetic and magnetocaloric effects of $La_{0.7}Sr_{0.3}Mn_{0.95}Ni_{0.05}O_3$ in different synthesis methods. *Journal of Electronic Materials* 2023; **52(4)**, 2665-2675.

[40] TM Al-Shahumi, IA Al-Omari, SH Al-Harthi and MTZ Myint. Synthesis, structure, morphology, magnetism, and magnetocaloric-effect studies of $(La_{1-x}Pr_x)_{0.7}Sr_{0.3}MnO_3$ nanocrystalline perovskites. *SN Applied Sciences* 2023; **5(4)**, 121.

[41] TM Al-Shahumi, IA Al-Omari, SH Al-Harthi, MTZ Myint, P Kharel, S Lamichhane and SH Liou. Synthesis, structure, morphology, magnetism, and magnetocaloric-effect studies of $La_{0.7}Sr_{0.3}Mn_{1-x}Fe_xO_3$ perovskite nanoparticles.

Journal of Alloys and Compounds 2023; **958**, 170454.

[42] M Khosrozadeh, K Mabhouti, P Norouzzadeh and R Naderali. Complex impedance spectroscopy, dielectric response, and magnetic properties of the $La_{0.7}Sr_{0.3}BO_3$ (B = Mn, Fe, Co, or Ni) perovskite oxides. *Ceramics International* 2024; **50(1)**, 315-328.

[43] IO Faniyi, O Fasakin, B Olofinjana, AS Adekunle, TV Oluwasusi, MA Eleruja and EOB Ajayi. The comparative analyses of reduced graphene oxide (RGO) prepared via green, mild and chemical approaches. *SN Applied Sciences* 2019; **1(10)**, 1181.

[44] PZZ Nehan, AA Akbar, MIN Karim, RA Fahriza and M Zainuri. Synthesis of silica from rice husk waste for hydrophobic material as an anti-water coating for eyeglasses. *Jurnal Fisika Dan Aplikasinya* 2023; **19(2)**, 44-48.

[45] B Uthaman, VR Akshay and MR Varma. Investigation on the structural, magnetic, magnetocaloric and magnetotransport behaviour of $La_{0.7}Sr_{0.3}MnO_3$ manganites synthesised by different routes. *Physical Chemistry Chemical Physics* 2024; **26(18)**, 13773-13789.

[46] M Houshiar, F Zebhi, ZJ Razi, A Alidoust and Z Askari. Synthesis of cobalt ferrite ($CoFe_2O_4$) nanoparticles using combustion, coprecipitation, and precipitation methods: A comparison study of size, structural, and magnetic properties. *Journal of Magnetism and Magnetic Materials* 2014; **371**, 43-48.

[47] PA Yadav, AV Deshmukh, KP Adhi, BB Kale, N Basavaih and SI Patil. Role of grain size on the magnetic properties of $La_{0.7}Sr_{0.3}MnO_3$. *Journal of Magnetism and Magnetic Materials* 2013; **328**, 86-90

[48] B Arun, VR Akshay and M Vasundhara. Observation of enhanced magnetic entropy change near room temperature in Sr-site deficient $La_{0.67}Sr_{0.33}MnO_3$ manganite. *RSC Advances* 2019; **9(41)**, 23598-23606.

[49] G Channagoudra, S Gupta and V Dayal. Study of structural, transport and magneto-crystalline anisotropy in $La_{1-x}Sr_xMnO_3$ ($0.30 \leq x \leq 0.40$) perovskite manganites. *AIP Advances* 2021; **11(2)**, 025305.

[50] MSI Sarker, U Salma, MNI Khan, MM Rahman and MKR Khan. Impact of annealing temperature on the structural, magnetic and dielectric properties of $BaFe_{12-x}Y_xO_{19}$ (x = 0.0, 0.2, 0.4, 0.6) nanocrystalline samples. *Ceramics International* 2024; **50(22)**, 45868-45879.

[51] H Zhang, D Zeng and Z Liu. The law of approach to saturation in ferromagnets originating from the magnetocrystalline anisotropy. *Journal of Magnetism and Magnetic Materials* 2010; **322(16)**, 2375-2380.

[52] R Topkaya. Effect of composition and temperature on the magnetic properties of $BaBi_xLa_xFe_{(12-2x)}O_{19}$ ($0.0 \leq x \leq 0.2$) hexaferrites. *Applied Physics A* 2017; **123(7)**, 488.

[53] G Dong, Y Liu, S Zhang, K Chu, H Li, X Pu, T Sun, F Ji and X Liu. Room-temperature TCR and low-field MR of $La_{0.7}Ca_{0.3-x}Sr_xMnO_3$ ($0.06 \leq x \leq 0.1$) polycrystalline ceramics. *Ceramics International* 2019; **45(17)**, 21448-21456.

[54] S Zhao, XJ Yue and X Liu. Influence of Sr doping on structural, electrical and magnetic properties of $La_{0.7}Ca_{0.3}MnO_3$ nanoparticles. *Ceramics International* 2017; **43(16)**, 13240-13246.

[55] PV Jithin, Y Bitla, MM Patidar, V Ganesan, KJ Sankaran and J Kurian. Structural, magnetic and electrical transport properties of the sol-gel derived $La_{1-x}Ca_xMnO_3$ ($0 \leq x \leq 0.3$) nanoparticles. *Materials Chemistry and Physics* 2023; **301**, 127651.

[56] SK Yadav, DP Pabba, A Soosairaj, K Divya, LR Asirvatham, VS Manikandan, M Navaneethan and A Thirumurugan. Study on the structural, magnetic, and magnetodielectric properties of M-type $BaFe_{12}O_{19}$ and $SrFe_{12}O_{19}$ hexaferrite nanoparticles. *Surfaces and Interfaces* 2024; **52**, 104956.

[57] R Dhahri, M Bejar, M Hajlaoui, N Sdiri, MA Valente and E Dhahri. Structural properties and electrical behaviour in the polycrystalline lanthanum-deficiency $La_{1-x}\square_xMnO_3$ manganites. *Journal of Magnetism and Magnetic Materials* 2009; **321(11)**, 1735-1738.